Energy Technology
Generation, Conversion, Storage, Distribution
www.entechnol.de

Visible-Light-Driven Electrocatalytic Oxygen Evolution Reaction: $NiFe_2O_4$/NiFe–Layered Double Hydroxide Z-Scheme Heteronanosheet as a Model

Lei Yan, Yanrong Ren, Junling Shen, Haiyan Wang, Jiqiang Ning, Yijun Zhong, and Yong Hu**

A visible-light-driven electronic structure regulation strategy is developed to boost the oxygen evolution reaction (OER) activity of the nickel ferrite ($NiFe_2O_4$)/NiFe–layered double hydroxide (LDH) electrocatalyst whose typical Z-scheme heterostructure makes it an ideal model to explore the mechanisms of photogenerated carriers in the electrocatalytic OER. The oxidation current of the composite increases significantly under visible light irradiation, resulting in a dramatic drop in the overpotential to 180 mV at a current density of 10 mA cm^{-2}. The Z-scheme heterostructure with efficient charge separation promotes photogenerated electron transfer from $NiFe_2O_4$ to NiFe–LDH, leading to the formation of an electron-rich Ni and Fe sites in NiFe–LDH and abundant photogenerated holes left in $NiFe_2O_4$, which are responsible for the improved electrocatalytic performance. Herein, the important role of photoactivated electron structure regulation in electrocatalysis is highlighted.

Electrocatalytic water splitting provides an efficient and sustainable approach for green hydrogen generation;[1–3] in particular, the anode oxygen evolution reaction (OER) with the multielectron and multiproton coupling steps features sluggish kinetics and large overpotentials of 300–500 mV, and thus, is generally regarded as the bottleneck for water splitting.[4,5] In this regard, efficient electrocatalysts that can accelerate O—H bond breaking and O—O bond formation are highly required.[6]

In the past decades, NiFe–layered double hydroxides (NiFe–LDHs) were acknowledged as the most promising alternatives to the benchmark RuO_2/IrO_2 catalyst in alkaline condition.[7,8] Enormous efforts have been devoted to activating the NiFe–LDH by electronic structure regulation of surface metals.[9,10] However, the positive results and methods are still limited and more importantly, the present catalysts still suffer from inferior OER activity and stability. As a result, a more simple and efficient strategy on electronic structure regulation is urgently required for further boosting the electrocatalytic OER performance of NiFe–LDH, and the corresponding regulation mechanism and effect are imperative to be recognized.

Lately, the plasmonic "hot electronics" emerged as an effective electron traps to modulate the electron density of active sites and optimize the electrochemical water-splitting performance.[11] For example, the pioneering work revealed that Au/$Ni(OH)_2$ nanosheets exhibited an superior OER performance under a 532 nm laser as a result of the Au surface plasmon resonance (SPR) activated $Ni^{III/IV}$ sites.[12] This work proved the potential of combining solar light and electricity for synergistically improving the electrocatalytic properties. Unfortunately, so far, most such works reported are limited to noble metals such as Au, Pt, and Pd, and their widespread uses are seriously restricted by the exorbitant prices and the low photochemical efficiencies.[13] As abundant and efficient solar harvests, transition metal oxides are widely utilized as photocatalysts whose light adsorption is closely associated with the nature bandgap.[14,15] Inspired by the aforementioned, we suggest that by integrating photochemical and electrochemical energy conversion system, the photogenerated carriers in transition metal oxides may be a convenient and effective way to tailor the electronic state of metal cations in NiFe–LDH and finally enhance the OER performance of the catalyst while to our knowledge, it has not been reported.

The key to optimize the photoinduced electrochemical OER activity is the rational design of stable NiFe–LDH/transition metal oxide heterostructures that match well with the band edge positions for accelerating the separation of photogenerated charge carriers and preventing the electron–hole recombination under visible light irradiation, and meanwhile facilitate more active metal species formation during the OER process.[16] Nickel ferrite ($NiFe_2O_4$), an n-type semiconductor, has recently attracted tremendous attention in photocatalysis, due to stable chemical and physical structure, wide adsorption in the visible

L. Yan, Y. Ren, J. Shen, Dr. H. Wang, Prof. Y. Zhong, Prof. Y. Hu
Key Laboratory of the Ministry of Education for Advanced Catalysis Materials
Department of Chemistry
Zhejiang Normal University
Jinhua 321004, China
E-mail: chemwhy@zjnu.edu.cn; yonghu@zjnu.edu.cn

Prof. J. Ning
Vacuum Interconnected Nanotech Workstation
Suzhou Institute of Nano-Tech and Nano-Bionics
Chinese Academy of Sciences
Suzhou 215123, China

The ORCID identification number(s) for the author(s) of this article can be found under https://doi.org/10.1002/ente.202000607.

DOI: 10.1002/ente.202000607

region, high adsorption capacity, and the necessary bandgap for water splitting.[17] Also, it presents a highly conductive structure due to the electron hopping between different valence metals in O-sites, which compensates for the low conductivity of NiFe–LDH.[18] Above all, with visible light irradiation, the charge separation at the $NiFe_2O_4$/NiFe–LDH heterogeneous interface can be accelerated under visible light irradiation, which may activate the metal active species and benefit the OER kinetics. Thus, it is an encouraging project to engineer a novel $NiFe_2O_4$/NiFe–LDH heterostructure and explore the photoactivated electronic structure regulation mechanisms for improving the electrocatalytic OER activity under visible light conditions.

As a proof of concept, in this article, we design a photoresponsive electrocatalyst based on $NiFe_2O_4$ decorated NiFe–LDH nanosheets and demonstrate that the surface electronic structure of NiFe–LDH can be modified to boost the OER performance of the catalyst under visible light irradiation. The Z-scheme $NiFe_2O_4$/NiFe–LDH heterostructure makes it an ideal model to explore the mechanisms of photogenerated carriers in the electrocatalytic OER. It has been discovered that the Z-scheme heterostructure promotes photogenerated electrons transfer from $NiFe_2O_4$ to NiFe–LDH upon visible light irradiation on catalysts, resulting in the increase in electron density of Ni and Fe in NiFe–LDH, as evidenced by the in situ irradiated X-ray photoelectron spectrum (XPS), UV–vis–diffused reflectance spectroscopy (UV–DRS), and Mott–Schottky (M–S) analyses. The electron-rich Ni and Fe sites can promote their early oxidation to higher valence states and facilitate the deprotonating step. In addition, the abundant photogenerated holes in the $NiFe_2O_4$ can also benefit the formation of highly active oxidative metal ions and the fast absorption of OH^- to the active sites. These factors together accelerated the OER kinetics and lowered the overpotential of catalyst to 180 mV at a current density of 10 mA cm^{-2}. The visible-light-driven electron structure regulation strategy thus provides a new and efficient avenue for optimizing the electrocatalytic activities.

The $NiFe_2O_4$/NiFe–LDH nanosheet arrays were prepared through a simple one-step hydrothermal reaction, as shown in Figure S1, See Supporting Information). The scanning electron microscopy (SEM) images reveal that 2D dense nanosheets grow vertically on the surface of Ni foam (NF) with a rough surface and a thickness of ≈50 nm (**Figure 1**a,b). The detailed structure of the

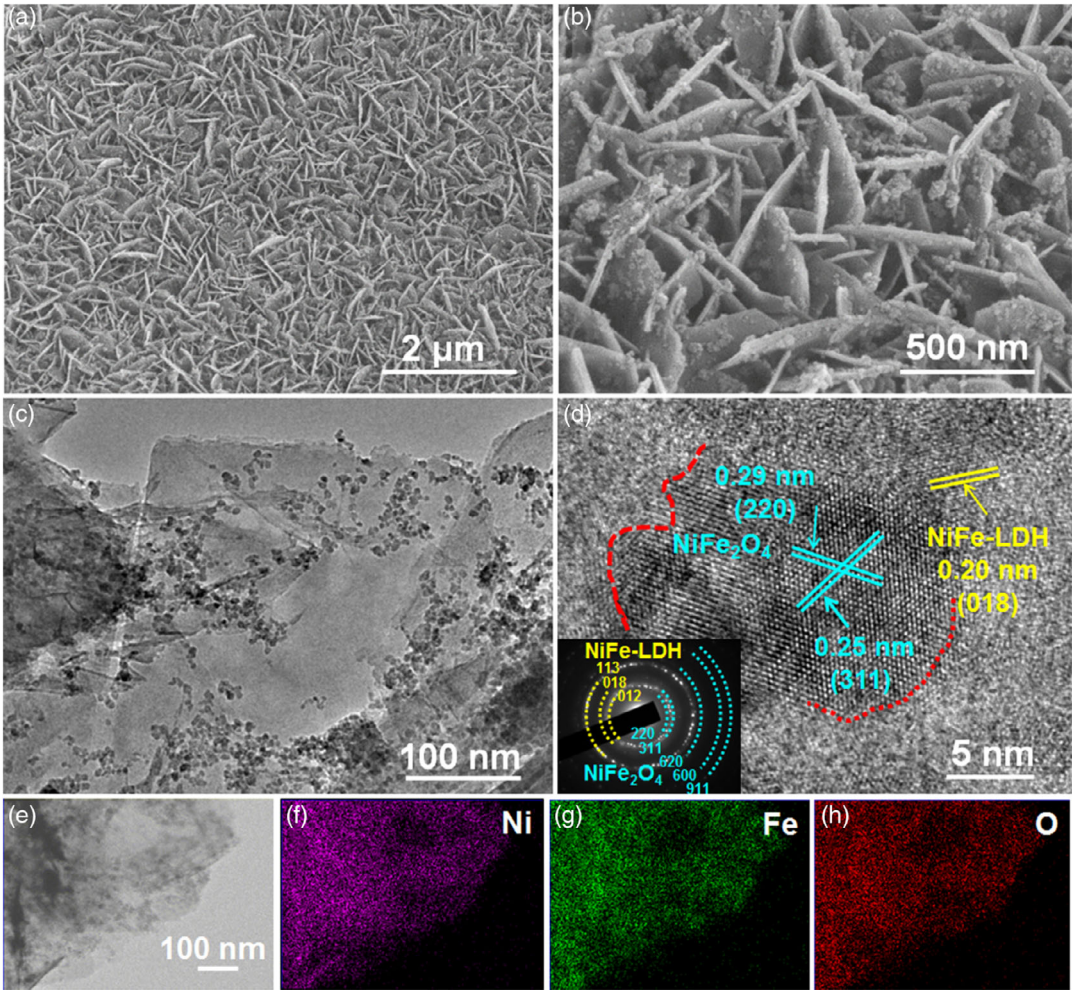

Figure 1. a,b) SEM, c) TEM, d) HRTEM, and e) scanning transmission electron microscopy images of $NiFe_2O_4$/NiFe–LDH. The elemental mapping images of f) Ni, g) Fe, and h) O elements in $NiFe_2O_4$/NiFe–LDH.

rough $NiFe_2O_4$/NiFe–LDH nanosheets was further investigated with transmission electron microscopy (TEM). The surfaces of the nanosheets are decorated with many nanoparticles, as shown in Figure 1c. The high-resolution TEM (HRTEM) image of these nanoparticle exhibits the lattice spacing of 0.29 nm and 0.25 nm, corresponding to the (220) and (311) lattice planes of $NiFe_2O_4$, respectively, and a lattice fringe of 0.20 nm is found, which can be assigned to the (018) facet of NiFe–LDH (Figure 1d). In addition, obvious interfaces of $NiFe_2O_4$ and NiFe–LDH are shown in the HRTEM image (red lines). The corresponding selected area electron diffraction (SAED) pattern with bright circles in the inset of Figure 1d can also be attributed to the different diffraction planes of $NiFe_2O_4$ and NiFe–LDH, further demonstrating the tight integration of NiFe–LDH and $NiFe_2O_4$. The elemental mapping images of $NiFe_2O_4$/NiFe–LDH reveal that Ni, Fe, and O elements are homogeneously distributed on the nanosheets and no other element is found (Figure 1e–h and Figure S2, Supporting Information). These results all proved that the $NiFe_2O_4$/NiFe–LDH heterostructure was well formed. For comparisons, the pure single components of NiFe–LDH and $NiFe_2O_4$ were fabricated (Figure S3 and S4, Supporting Information).

The phase composition and purity of $NiFe_2O_4$/NiFe–LDH heterostructure were analyzed by powder X-ray diffraction (XRD) and Raman spectroscopy. The diffraction peaks located at 44.5°, 51.8°, and 76.4° correspond to the Ni, whereas the other peaks are assigned to $NiFe_2O_4$ (JCPDS No. 86-2267) and NiFe–LDH (JCPDS No. 40-0215) (**Figure 2**a). The Raman spectrum in Figure 2b shows the peaks centered at 196, 330, and 701 cm^{-1} which are indexed to the T_{2g}, E_g, and A_{1g} modes of $NiFe_2O_4$.[19] The peaks at 456 and 534 cm^{-1} are assigned to the Ni—O stretching of NiFe–LDH, and the 295 cm^{-1} signal is attributed to the E-type vibration of the Ni—OH lattice,[20] which echo well with the spectrum obtained by pure NiFe–LDH. These results fully demonstrated that the as-obtained structure is a composite of $NiFe_2O_4$ and NiFe–LDH without any impurities.

XPS measurements were further performed to confirm the chemical compositions and valences of the $NiFe_2O_4$/NiFe–LDH catalyst. The survey spectrum demonstrates the presence of Ni, Fe, and O elements in the as-prepared samples (Figure S5, Supporting Information). The Ni 2p XPS spectra can be fitted into two spin-orbit doublets and two shake-up satellites (Figure 2c). The peaks at 855.3 and 873.1 eV correspond to Ni^{2+}, whereas the peaks at 856.5 and 874.6 eV are attributed to Ni^{3+}.[21] For the XPS spectrum of Fe 2p, the peaks at 712.3 and 724.7 eV are assigned to Fe^{3+} species (Figure 2d).[22,23] In addition, the Ni 2p XPS and Fe 2p XPS spectra in $NiFe_2O_4$/NiFe–LDH both exhibit positive shifts relative to those for $NiFe_2O_4$, but negative shifts concerning the peaks of NiFe–LDH, confirming that electrons transferred from $NiFe_2O_4$ to NiFe–LDH in $NiFe_2O_4$/NiFe–LDH.[24] To evaluate the feasibility of $NiFe_2O_4$/NiFe–LDH heterostructure in the photoenhanced electrocatalytic system, the optical absorption capability of the electrode was first investigated by UV–DRS. As shown in Figure S6, Supporting Information), $NiFe_2O_4$/NiFe–LDH exhibits a strong adsorption at the visible region which is much higher than that of $NiFe_2O_4$ and NiFe–LDH samples, indicating the excellent light-harvesting property of $NiFe_2O_4$/NiFe–LDH. Thus,

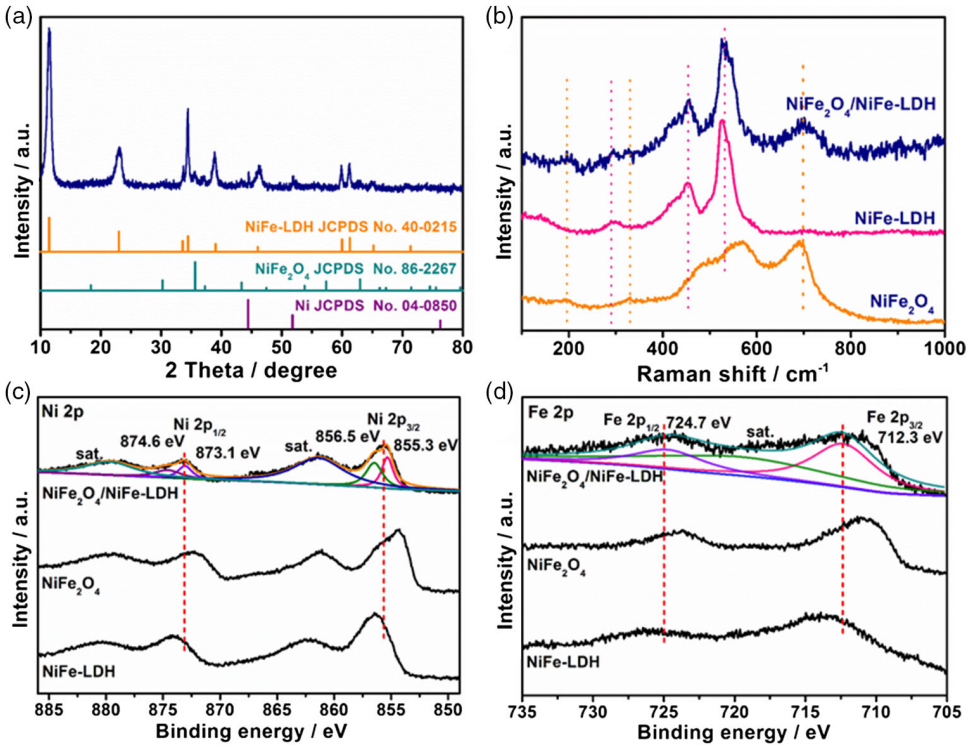

Figure 2. a) XRD pattern of $NiFe_2O_4$/NiFe–LDH. b) Raman spectra, c) high-resolution Ni 2p XPS spectra, and d) Fe 2p XPS spectra of $NiFe_2O_4$/NiFe–LDH, $NiFe_2O_4$, and NiFe–LDH catalysts.

$NiFe_2O_4$/NiFe–LDH might be a promising catalyst to explore the photoenhanced electrochemical properties and the electrocatalytic OER performance was then performed in 1.0 M KOH solution by measuring polarization curves in a three-electrode system with or without simulated visible light irradiation. As comparisons, the pure $NiFe_2O_4$ and NiFe–LDH samples were also tested under the same conditions. In the dark, the $NiFe_2O_4$/NiFe–LDH heterostructure shows an overpotential of 206 mV at 10 mA cm^{-2}, much lower than those of NiFe–LDH (231 mV) and $NiFe_2O_4$ (334 mV) catalysts (**Figure 3**a). The superior OER performance of $NiFe_2O_4$/NiFe–LDH to $NiFe_2O_4$ and NiFe–LDH catalysts can be due to the largest electrochemical active surface area of $NiFe_2O_4$/NiFe–LDH (Figure S7, Supporting Information), and the electronic interaction at the $NiFe_2O_4$/NiFe–LDH interface which increased the electron density in NiFe–LDH and produced the highly oxidative Ni and Fe in $NiFe_2O_4$, and thus boosted the OER kinetics and improved the OER activity.[25] After exposed to visible light at room temperature, an improvement of the OER activity was observed for all catalysts. Specifically, $NiFe_2O_4$/NiFe–LDH (light) delivers only 180 and 231 mV to achieve the current densities of 10 and 100 mA cm^{-2}, which is superior to most those reported for the NiFe–LDH-based OER catalysts (Table S1, Supporting Information). Remarkably, compared to that of $NiFe_2O_4$/NiFe–LDH, the overpotential of $NiFe_2O_4$/NiFe–LDH (light) at 100 mA cm^{-2} decreases dramatically by 47 mV (Figure 3b). In contrast, NiFe–LDH (light) and $NiFe_2O_4$ (light) require overpotentials of 294 mV and 430 mV to reach 100 mA cm^{-2} which are 22 and 13 mV lower than those in the dark, respectively. These phenomena implied that the photopromoted OER performance of $NiFe_2O_4$/NiFe–LDH heterostructure was not just a simple summation of the two results of $NiFe_2O_4$ and NiFe–LDH, but can be a synergistic effect of the two components.

To have a preliminary of this phenomenon, Tafel plots of the three samples were analyzed based on their OER polarization curves. Similarly, $NiFe_2O_4$/NiFe–LDH heterostructure exhibits a Tafel value of 49.3 mV dec^{-1}, smaller than 64.2 mV dec^{-1} of NiFe–LDH and 71.4 mV dec^{-1} of $NiFe_2O_4$ (Figure 3c), indicating a faster OER kinetics for $NiFe_2O_4$/NiFe–LDH. Under visible light irradiation, the Tafel slope of $NiFe_2O_4$/NiFe–LDH (light) decreases significantly to 40.6 mV dec^{-1}, demonstrating that visible light irradiation accelerates the OER kinetics, and therefore, improves the OER activity of $NiFe_2O_4$/NiFe–LDH catalyst. As shown in Figure S8, Supporting Information), higher turnover frequencies (TOFs) of 0.071 and 0.175 s^{-1} are achieved for $NiFe_2O_4$/NiFe–LDH at the overpotentials of 400 and 500 mV under visible light irradiation, being 1.1 and 1.29 times those of $NiFe_2O_4$/NiFe–LDH without light, respectively, further confirming that visible light can improve the intrinsic activity of $NiFe_2O_4$/NiFe–LDH electrocatalyst. In addition, the chronopotentiometric response of $NiFe_2O_4$/NiFe–LDH catalyst with light irradiation on and off reveals that visible light irradiation causes an obvious decrease in the potential, further manifesting the improvement of the OER activity (Figure 3d). The electrochemical impedance spectroscopy (EIS) measurement was also used to give a better understanding of the charge-transfer kinetics of

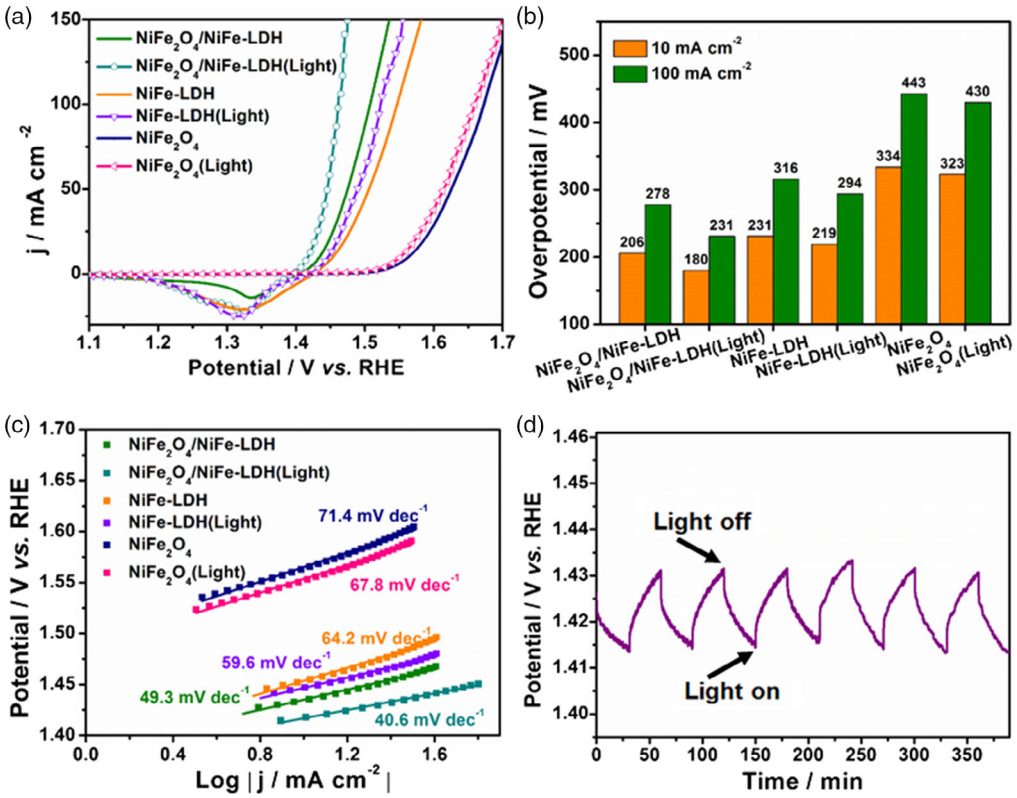

Figure 3. a) OER polarization curves, b) overpotentials at 10 and 100 mA cm^{-2}, and c) Tafel slopes of $NiFe_2O_4$/NiFe–LDH, $NiFe_2O_4$, and NiFe–LDH in 1.0 M KOH solution with or without light irradiation. d) Chronopotentiometric stability test of $NiFe_2O_4$/NiFe–LDH with visible light irradiation on and off.

catalysts. The results show that $NiFe_2O_4$/NiFe–LDH (light) has the smallest charge-transfer resistance (R_{ct}) of 1.38 Ω, suggesting the enhanced charge transport efficiency (Figure S9a and Table S2, Supporting Information). Remarkably, the $NiFe_2O_4$/NiFe–LDH (light) displays a negligible increase in potential during the chronopotentiometric stability test for more than 30 h (Figure S9b, Supporting Information), and the polarization curve after the stability test also shows the slight decrease compared to the initial test (Figure S10, Supporting Information). Furthermore, the morphology and structure have little change (Figure S11 and S12, Supporting Information), indicating the promise of adopting the long-term stable $NiFe_2O_4$/NiFe–LDH as a high-performance photopromoted OER catalyst.

Further to have an in-depth insight into the enhancement effect of light on water oxidation performance of $NiFe_2O_4$/NiFe–LDH catalyst, M–S analysis was first performed on $NiFe_2O_4$ and NiFe–LDH. As shown in **Figure 4**a,b, $NiFe_2O_4$ and NiFe–LDH both exhibit the positive slope in the M–S plots, indicating the n-type semiconductor properties. The Kubelka–Munk plots of $NiFe_2O_4$ and NiFe–LDH were obtained using the UV–DRS (Figure S13, Supporting Information). The bandgaps are 1.51 eV and 1.72 eV for the $NiFe_2O_4$ and NiFe–LDH, respectively. In addition, the $NiFe_2O_4$/NiFe–LDH catalyst displays a more significant increase in the photocurrent responses (about 0.28 mA cm^{-2}) at 1.2 V under pulsed light irradiation (Figure S14, Supporting Information), much larger than those of NiFe–LDH (0.06 mA cm^{-2}), and $NiFe_2O_4$ (0.04 mA cm^{-2}), manifesting that the photoinduced electron–hole pairs in $NiFe_2O_4$/NiFe–LDH catalyst are more easy to separate and transfer, and thus can enhance electronic regulation at the $NiFe_2O_4$/NiFe–LDH interface.

For a direct illustration of the photoexcited electron transfer direction between $NiFe_2O_4$ and NiFe–LDH, in situ irradiated XPS was conducted under irradiation. As shown in Figure 4c,d,

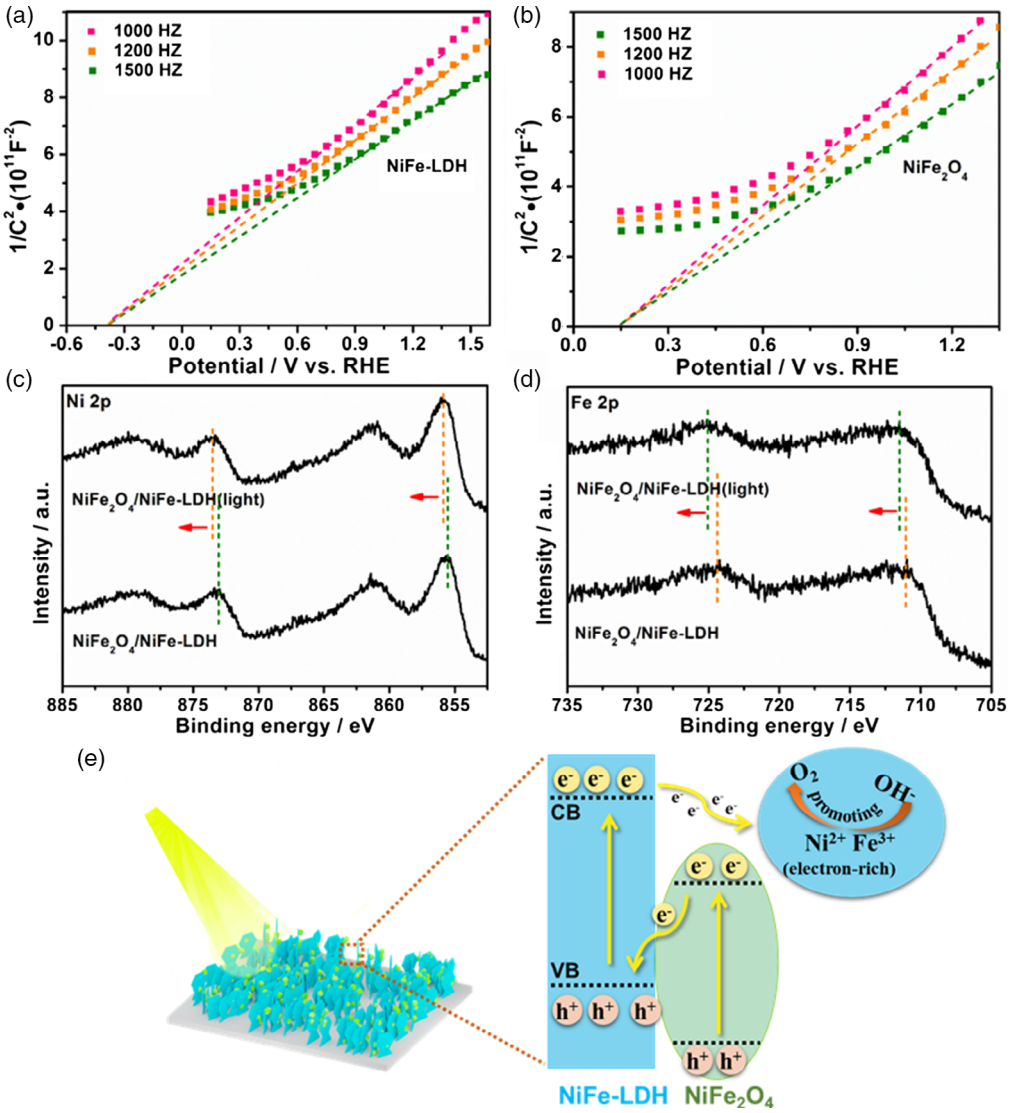

Figure 4. M–S plots with frequency at 1.0, 1.2, and 1.5 kHz of a) NiFe–LDH and b) $NiFe_2O_4$. High-resolution c) Ni 2p and d) Fe 2p XPS spectra of $NiFe_2O_4$/NiFe–LDH in the dark or under light irradiation. e) Schematic graphs illustrating photoinduced electron transfer mechanism of $NiFe_2O_4$/NiFe–LDH.

the electron-binding energy of Ni 2p and Fe 2p in $NiFe_2O_4$/NiFe–LDH (light) both increases compared with the pristine $NiFe_2O_4$/NiFe–LDH catalyst, which indicates that the charge carrier migration pathway from $NiFe_2O_4$ to NiFe–LDH is enhanced under light irradiation condition.[26,27] The photogenerated electrons' transfer leads to a further increase in the electronic densities of Ni and Fe in NiFe–LDH and more abundant photogenerated holes left to oxidize $NiFe_2O_4$. By contrast, no obvious change can be observed in the binding energies for the $NiFe_2O_4$ and NiFe–LDH with/without light irradiation, respectively, (Figure S15, Supporting Information). Based on the aforementioned results, the Z-scheme photogenerated electrons transfer mechanism of $NiFe_2O_4$/NiFe–LDH for enhancing the electrocatalytic OER process is proposed (Figure 4e). The bandgap level analysis reveals that conduction band (CB) and valance band (VB) positions are ≈0.15 and 1.66 V for $NiFe_2O_4$, respectively, and −0.38 eV and 1.34 eV for NiFe–LDH, respectively. Similarly, the bandgap value and VB potential of $NiFe_2O_4$/NiFe–LDH is about 1.57 eV and 0.03 V, respectively, (Figure S16, Supporting Information). Under visible light irradiation, photoinduced electron–hole pairs are generated in NiFe–LDH and $NiFe_2O_4$. The photogenerated electrons are transferred from $NiFe_2O_4$ to NiFe–LDH, resulting in an efficient space separation of photoinduced charge carriers.[28,29] The accelerated electron transfer endows NiFe–LDH with electron-rich Ni and Fe promote their early oxidation to higher valence states and facilitate the deprotonating step.[30] Meanwhile, due to the relative low VB position of $NiFe_2O_4$ is more negative than the potential of water oxidation, the abundant photogenerated holes stored in $NiFe_2O_4$ cannot oxidize water to oxygen, but are beneficial for the formation of highly oxidative metal ions and may accelerate the fast absorption of OH^- to the active sites.[31,32] These factors combined promoted the OER kinetics and enhance the OER performance of $NiFe_2O_4$/NiFe–LDH.

In summary, an effective strategy was proposed to regulate the surface electronic structure of NiFe–LDH for enhanced OER performance by visible light irradiation. A photoresponsive electrocatalyst of Z-scheme $NiFe_2O_4$/NiFe–LDH heterostructure is designed and prepared. The in situ irradiated XPS, UV–DRS, and electrochemical results all confirm that great improvement in OER activity relies on the photoenhanced efficient electron transfer from $NiFe_2O_4$ to NiFe–LDH as a result of the Z-scheme heterostructure. This work provides an insight into the visible-light-driven electron structure regulation for high-performance OER, which may open a new way for the design and synthesis of efficient photoresponsive Z-scheme electrocatalysts toward much broader energy-related applications.

Experimental Section

Synthesis of $NiFe_2O_4$/NiFe–LDH: All reagents used in this article were analytical grade without further purification, purchased from Shanghai Chemical Reagent Factory. Typically, $Fe(NO_3)_3{\cdot}9H_2O$ (0.5 mmol, 202 mg) and urea (10 mmol, 600 mg) were dissolved with a 35 mL of distilled water (35 mL). The obtained solution was then moved to a 45 mL Teflon-lined stainless steel autoclave. Before immersed into the aforementioned autoclave, the NF (2 × 3 cm) was cleaned with 3 M HCl and distilled water for 20 min. Then, the autoclave was heated at 120 °C for 10 h before the system was cooled down. The product was washed with deionized water and ethanol for several times and then vacuum dried overnight. The mass loading of $NiFe_2O_4$/NiFe–LDH was about 0.8 mg cm^{-2}.

Synthesis of NiFe–LDH: The NiFe–LDH was synthesized by the same method as $NiFe_2O_4$/NiFe–LDH, but $Ni(NO_3)_2{\cdot}6H_2O$ (1.5 mmol, 437 mg) was added.

Synthesis of $NiFe_2O_4$: $NiFe_2O_4$/NiFe–LDH grown on NF was heated at 450 °C for 2 h under an air atmosphere with a heating rate of 2 °C min^{-1} to obtain $NiFe_2O_4$.

Material Characterizations: The crystal structures of the products were characterized by XRD measurements with a Bruker D8 Advance X-ray diffractometer using a Cu Kα radiation source with a velocity of 12 min^{-1}. SEM measurements were collected on a Hitachi S-4800 scanning electron microanalyzer with an accelerating voltage of 15 kV, combined with an energy dispersive X-ray spectroscopy (EDS) mapping to investigate the elemental distribution of the samples. TEM and HRTEM images were performed on a JEM-2100 F field-emission TEM at a voltage of 200 kV. The surface element properties of the samples were investigated by XPS using an ESCALab MKII X-ray photoelectron spectrometer with Mg Kα X-ray as the excitation source. Raman spectra were obtained from a micro Raman spectrometer (Renishaw RM 1000) at an excitation laser wavelength of 532 nm. UV–DRS tests were recorded over the range of 200–800 nm in the absorption mode of a Thermo Nicolet Evolution 500 UV–vis spectrophotometer equipped with an integrating sphere attachment.

Electrochemical Measurements: The electrochemical experiments were conducted in 1.0 M KOH solution (pH = 13.6) at room temperature using a bipotentiostat workstation (WD20-BASIC Metrohm PGSTAT101) with a three-electrode electrochemical cell system. In the three-electrode system, the catalyst electrodes were directly used as the working electrodes, saturated calomel electrode (SCE, saturated KCl) as the reference electrode, and a graphite rod as the counter electrode. The polarization profiles were obtained through linear sweep voltammetry (LSV) with a scan rate of 2 mV s^{-1}. EIS measurements were recorded at a current density of 10 mA cm^{-2} on a Zennium electrochemical workstation (ZAHNER, Germany) with a frequency range from 10^5 to 0.1 Hz. The electrochemical double layer capacitance (C_{dl}) of working electrodes was made by using cyclic voltammetry (CV) scanning with scanning rates of 20, 40, 60, 80, and 100 mV s^{-1}. All potentials of the polarization curves were adjusted to compensate for the ohmic potential drop losses that arose from the solution resistance and calibrated with respect to reversible hydrogen electrode (RHE).

$$E_{RHE} = E_{SCE} + 0.242 + 0.059 \times pH - 0.9 \times iR \quad (1)$$

The values of TOF were calculated according to Equation (2).

$$TOF = \frac{j \times s_{geo}}{4F \times n} \quad (2)$$

where j is the current density of catalysts on a glassy carbon (GC) electrode at an overpotential of 400 and 500 mV, S_{geo} the area of the GC, F the Faraday constant (96 485 C mol^{-1}), and n is the moles of Ni and Fe atoms on the electrode which can be calculated by the loading weight of the coated catalysts. The M–S measurement performed at a frequency of 1, 1.2, and 1.5 kHz with 10 mV amplitude was used, with various applied potentials on a Zennium electrochemical workstation using a standard three-electrode cell with 0.5 M Na_2SO_4 electrolyte solution in a three-electrode quartz cell with catalyst electrodes as the working electrode, a platinum wire as counter electrode, and SCE as the reference electrode. Photocurrent measurements were performed on a CHI660E electrochemical workstation in the same three-electrode configuration at the 1.2 V bias potential versus SCE in a 1.0 M Na_2SO_4 aqueous solution. A 300 W Xe lamp (Microsolar 300, Perfect Light) with a cut-on filter ($\lambda > 420$ nm) was used as the visible light source, and the distance between electrode and Xe lamp was about 5 cm.

Supporting Information

Supporting Information is available from the Wiley Online Library or from the author.

Acknowledgements

L.Y. and Y.R. contributed equally to this work. Y.H. acknowledges the financial support from Natural Science Foundation of China (21671173) and Zhejiang Provincial Ten Thousand Talent Program (2017R52043).

Conflict of Interest

The authors declare no conflict of interest.

Keywords

$NiFe_2O_4$, NiFe–layered double hydroxides, oxygen evolution reaction, photoresponsive electrocatalysis, Z-scheme heterostructures

Received: July 2, 2020
Revised: September 14, 2020
Published online: October 20, 2020

[1] Y. Jiao, Y. Zheng, M. Jaroniec, S. Z. Qiao, *Chem. Soc. Rev.* **2015**, *44*, 2060.
[2] H. Wang, Y. Yang, Q. Li, W. Lu, J. Ning, Y. Zhong, Z. Zhang, Y. Hu, *Sci. China Mater.* https://doi.org/10.1007/s40843-020-1476-2.
[3] L. Yan, H. Wang, J. Shen, J. Ning, Y. Zhong, Y. Hu, *Chem. Eng. J* **2021**, *403*, 126385.
[4] Y. Liang, Y. Li, H. Wang, J. Zhou, J. Wang, T. Regier, H. Dai, *Nat. Mater.* **2011**, *10*, 780.
[5] J.-C. Li, P.-X. Hou, S.-Y. Zhao, C. Liu, D. M. Tang, M. Cheng, F. Zhang, H.-M. Cheng, *Energy Environ. Sci.* **2016**, *9*, 3079.
[6] J. Wang, Z. Huang, W. Liu, C. Chang, H. Tang, Z. Li, W. Chen, C. Jia, T. Yao, S. Wei, Y. Wu, Y. Li, *J. Am. Chem. Soc.* **2017**, *139*, 17281.
[7] P. Li, X. Duan, Y. Kuang, Y. Li, G. Zhang, W. Liu, X. Sun, *Adv. Energy Mater.* **2018**, *8*, 1703341.
[8] D. Zhao, Y. Pi, Q. Shao, Y. Feng, Y. Zhang, X. Huang, *ACS Nano* **2018**, *12*, 6245.
[9] G. Chen, T. Wang, J. Zhang, P. Liu, H. Sun, X. Zhuang, M. Chen, X. Feng, *Adv. Mater.* **2018**, *30*, 1706279.
[10] L. Yan, Y. Ren, X. Zhang, Y. Sun, J. Ning, Y. Zhong, B. Teng, Y. Hu, *Nanoscale* **2019**, *11*, 20797.
[11] M. Wang, P. Wang, C. Li, H. Li, Y. Jin, *ACS Appl. Mater. Interfaces* **2018**, *10*, 37095.
[12] L. Du, G. Shi, Y. Zhao, X. Chen, H. Sun, F. Liu, F. Cheng, W. Xie, *Chem. Sci.* **2019**, *10*, 9605.
[13] Z. Zheng, W. Xie, M. Li, Y. H. Ng, D.-W. Wang, Y. Dai, B. Huang, R. Amal, *Nano Energy* **2017**, *41*, 233.
[14] R. Marschall, L. Wang, *Catal. Today* **2014**, *225*, 111.
[15] Q. Lu, Y. Yu, Q. Ma, B. Chen, H. Zhang, *Adv. Mater.* **2016**, *28*, 1917.
[16] S. Nayak, L. Mohapatra, K. Parida, *J. Mater. Chem. A* **2015**, *3*, 18622.
[17] W. Fu, X. Xu, W. Wang, J. Shen, M. Ye, *ACS Sustain. Chem. Eng.* **2018**, *6*, 8935.
[18] M. Li, Y. Xiong, X. Liu, X. Bo, Y. Zhang, C. Han, L. Guo, *Nanoscale* **2015**, *7*, 8920.
[19] A. Ahlawat, V. G. Sathe, *J. Raman Spectrosc.* **2011**, *42*, 1087.
[20] D. Zhou, S. Wang, Y. Jia, X. Xiong, H. Yang, S. Liu, J. Tang, J. Zhang, D. Liu, L. Zheng, Y. Kuang, X. Sun, B. Liu, *Angew. Chem. Int. Ed.* **2019**, *58*, 736.
[21] A. T. Swesi, J. Masud, M. Nath, *Energy Environ. Sci.* **2016**, *9*, 1771.
[22] C. Tang, R. Zhang, W. Lu, L. He, X. Jiang, A. M. Asiri, X. Sun, *Adv. Mater.* **2017**, *29*, 1602441.
[23] J. Hu, S. W. Li, J. Y. Chu, S. Q. Niu, J. Wang, Y. C. Du, Z. H. Li, X. J. Han, P. Xu, *ACS Catal.* **2019**, *9*, 10705.
[24] H. Yan, Y. Xie, A. Wu, Z. Cai, L. Wang, C. Tian, X. Zhang, H. Fu, *Adv. Mater.* **2019**, *31*, 1901174.
[25] Z. W. Gao, J. Y. Liu, X. M. Chen, X. L. Zheng, J. Mao, H. Liu, T. Ma, L. Li, W. C. Wang, X. W. Du, *Adv. Mater.* **2019**, *31*, 1804769.
[26] J. Low, B. Dai, T. Tong, C. Jiang, J. Yu, *Adv. Mater.* **2019**, *31*, 1802981.
[27] L. Li, C. Guo, J. Shen, J. Ning, Y. Zhong, Y. Hu, *Chem. Eng. J* **2020**, *400*, 125925.
[28] W. Zhao, Y. Feng, H. B. Huang, P. C. Zhou, J. Li, L. L. Zhang, B. L. Dai, J. M. Xu, F. X. Zhu, N. Sheng, D. Y. C. Leung, *Appl. Catal. B-Environ.* **2019**, *245*, 448.
[29] Y. Z. Hong, Y. H. Jiang, C. S. Li, W. Q. Fan, X. Yan, M. Yan, W. D. Shi, *Appl. Catal. B-Environ.* **2016**, *180*, 663.
[30] D. J. Zhou, Z. Cai, Y. Jia, X. Y. Xiong, Q. X. Xie, S. Y. Wang, Y. Zhang, W. Liu, H. H. Duan, X. M. Sun, *Nanoscale Horiz.* **2018**, *3*, 532.
[31] J. Xu, P. Gu, D. Birch, Y. Chen, *Adv. Funct. Mater.* **2018**, *28*, 1801573.
[32] S. Li, P. Miao, Y. Zhang, J. Wu, B. Zhang, Y. Du, X. Han, J. Sun, P. Xu, *Adv. Mater.* **2020**, 2000086.